ORIGINAL ARTICLE

Functional balance between Tcf21–Slug defines cellular plasticity and migratory modalities in high grade serous ovarian cancer cell lines

Sagar S.Varankar, Madhuri More, Ancy Abraham, Kshama Pansare[1], Brijesh Kumar, Nivedhitha J.Narayanan, Mohit Kumar Jolly[2,3], Avinash M.Mali and Sharmila A.Bapat[*],[ⓞ]

National Centre for Cell Science, Savitribai Phule Pune University, Ganeshkhind, Pune 411007, India, [1]Institute for Plasma Research & Tata Memorial Centre, Kharghar, Navi-Mumbai, India and [2]Center for Theoretical Biological Physics, Rice University, Houston, TX, USA [3]Present addresses: Centre for Biosystems Science and Engineering, Indian Institute of Science, Bangalore 560012, India.

[*]To whom correspondence should be addressed. Tel: +91 020 25708089; Fax: +91 20 25692259; Email: sabapat@nccs.res.in

Abstract

Cellular plasticity and transitional phenotypes add to complexities of cancer metastasis that can be initiated by single cell epithelial to mesenchymal transition (EMT) or cooperative cell migration (CCM). Our study identifies novel regulatory cross-talks between Tcf21 and Slug in mediating phenotypic and migration plasticity in high-grade serous ovarian adenocarcinoma (HGSC). Differential expression and subcellular localization associate Tcf21, Slug with epithelial, mesenchymal phenotypes, respectively; however, gene manipulation approaches identify their association with additional intermediate phenotypic states, implying the existence of a multistep epithelial-mesenchymal transition program. Live imaging further associated distinct migratory modalities with the Tcf21/Slug status of cell systems and discerned proliferative/passive CCM, active CCM and EMT modes of migration. Tcf21–Slug balance identified across a phenotypic spectrum in HGSC cell lines, associated with microenvironment-induced transitions and the emergence of an epithelial phenotype following drug exposure. Phenotypic transitions and associated functionalities following drug exposure were affirmed to ensue from occupancy of Slug promoter E-box sequences by Tcf21. Our study effectively provides a framework for understanding the relevance of ovarian cancer plasticity as a function of two transcription factors.

Introduction

Intrinsic cellular identities originate during embryonic commitment and are fated for tissue specific spatiotemporal roles through cross-talks with niche components (1). Destabilization of homeostasis under pathological conditions alters the tissue milieu to revoke inherent cellular plasticity and restore primitive phenotype(s), architecture and functions to facilitate disease progression (2,3). Cooperative action of regulatory molecular circuits such as the role of Slug–Sox9 in maintenance of mammary basal and luminal epithelial cells, are diverted in aberrant contexts like cell transformation to redefine cell fates

(4,5). Innate capabilities and perturbed microenvironment thus align as distinct etiologies in cancer (6,7). Previous studies in epithelial ovarian carcinomas (EOC) identified Stem-A, Stem-B, Epi-A, Epi-B and Mes subtypes that correspond with epithelial (E), intermediate epithelial (iE), intermediate mesenchymal (iM) and mesenchymal (M) phenotypic features (8,9); a subsequent study reported iE and iM as extensions of an epithelial-mesenchymal hybrid state (EM). Furthermore, comprehensive analyses of the most aggressive EOC *viz.* high-grade serous adenocarcinomas (HGSC) have revealed diverse molecular signatures that

Abbreviations

aCCM active collective cell migration
BMP7 bone morphogenetic protein 7
CCM cooperative cell migration
Cdh1 E-cadherin
E epithelial
EM epithelial-mesenchymal hybrid
EMT epithelial to mesenchymal transition
HGSC high grade serous carcinoma
iE intermediate epithelial
iM intermediate mesenchymal
K/O knock-out
M mesenchymal
Nn nearest neighbors
OE overexpression
pCCM passive collective cell migration
SS serum starved
TCGA The Cancer Genome Atlas
TF transcription factors
TGFβ transforming growth factor β
Vim vimentin

correlate with epithelial/differentiated (E/D), mesenchymal (M), proliferative (P), immunoreactive (IR) features and require adoption of differential therapeutic strategies (10–13). Hence, the disparate collation of EOC datasets can misrepresent the clinical associations of tumor subtypes with phenotypic states and should be avoided to improve disease management.

Our previous analyses of HGSC expression datasets in The Cancer Genome Atlas (TCGA) resolved three molecular subclasses associated with discrete mechanisms of metastases. Class 1 exhibited cooperative cell migration (CCM), Class 2 associated with epithelial-mesenchymal transitions (EMT) while Class 3 presented with mixed features (11,14). Correlating with reports using the same datasets suggested CCM-Class tumors to present as P/D/iE subclass, EMT-Class tumors as M/IR/iM while the heterogeneous Class 3 tumors possibly represent IR/D phenotypes. While molecular signatures for HGSC subtypes have been defined across multiple studies, the limited comprehension of aberrantly activated plasticity programs curb effective translation of previous findings. In the present study, we discern HGSC cell phenotypes (E/M/intermediates) as a function of Tcf21 and Slug expression, localization and activity. Functional evaluation assisted by real-time imaging, associated phenotypic states with either EMT, active CCM or proliferative (annotated as passive CCM/pCCM) modes of wound closure. As opposed to the rigidity of epithelial/mesenchymal phenotypes, intermediate states exhibited transitions between EMT and, active collective cell migration (aCCM) (but not pCCM) modalities and responded with enhanced plasticity in presence of positive/negative growth regulators as a function of altered Tcf21–Slug subcellular localization. Strikingly, emergence of epithelial features involved transcriptional repression of Slug by Tcf21. Our study thus, highlights the antagonistic interplay of Tcf21–Slug in maintenance of distinct cellular phenotypes and presents them as potential biomarkers for phenotype-assisted tumor stratification.

Materials and methods

Cell culture

Ovarian cancer cell lines used in the study were all of the high grade serous histology (15,16). A4 cells were previously established in our lab from ascites of a HGSC patient (17), OVCAR3 cells were obtained from the cell repository at NCCS, Pune, India. Dr S. Mok (M. D. Anderson Cancer Center, TX) and Prof. Viktor Magdalen (Klinische Forschergruppe der Frauenklinik der TU München) provided OV90 and OVMZ6 cell lines, respectively. OVCA420, PEO14, OVCA432 and CAOV3 cells were provided by Prof. Judith Clements (Translational Research Institute, Australia). OVCAR3, OVCA432, CAOV3, OV90, OVCA420 and PEO14 cells were grown in RPMI 1640 (Gibco, Waltham, MA) supplemented with 10% fetal bovine serum. A4 cells were cultured in Minimal Essential Medium/MEM (Gibco) supplemented with 5% fetal bovine serum and 1% nonessential amino acids; Dulbecco's Modified Essential Medium/DMEM (Gibco) supplemented with 5% serum, 100 μM asparagine (Sigma, St. Louis, MO) and 100 μM arginine (Sigma) was used for culturing OVMZ6 cells. All cell lines were maintained in a humidified incubator at 37°C under a 5% CO_2 atmosphere. Cell lines were authenticated by short tandem repeat profiling and comparison with ATCC and EACC databases (June 2018).

Transfection, generation of TF derivative clones

For generation of knockouts via genomic editing OVCAR3 and A4 cells were transfected with 500 ng of commercially available CrispR_GFP vectors against Tcf21 and Slug (Sigma), respectively using Lipofectamine 3000 (Invitrogen, Carlsbad, CA) as per the manufacturer's protocol. Post transfection, cells were incubated at 30°C for 48 h to ensure optimal CrispR activity that was confirmed by the T7 endonuclease assay (data not provided). Single cell sorting of GFP positive cells was performed with BD Aria II SORP into 96 well plates. Sorted cells were allowed to grow for clone establishment and subjected to molecular (qPCR, immunoblotting, immunofluorescence staining) and functional (*in vitro* wound closure) validation. Successful knockouts (E2–Tcf21 knockout, D7–Slug knockout) obtained from CrispR transfections, were further transfected with GFP vectors for Slug and Tcf21, respectively, sorted to obtain single cell clones and validated. Tcf21$^{K/O}$Slug^{OE} clones could not be established due to rapid apoptosis.

Treatments

Cells were treated as follows before RNA extraction and immunofluorescence staining:
Serum deprivation: cells were allowed to grow for 24 h post-seeding, following which spent medium for each cell line was replaced with equal volume of serum free media as indicated for each cell line. *Growth factor exposure:* 24 h following serum deprivation, cell lines were exposed to either bone morphogenetic protein 7 (BMP7) (10 ng/ml), TGFβ (10 ng/ml) or a combination of both (Invitrogen). *Paclitaxel treatment:* cells were allowed to grow for 24 h post-seeding, after which spent medium for each cell line was replaced with equal volume of complete medium containing IC50 concentrations of paclitaxel (Sigma) optimized for each cell line (IC50 values for each cell line are available on request). 0.1% DMSO was used as a vehicle control.

Derivation of TF network, correlation and expression analysis of TFs and phenotypic markers in TCGA–HGSC dataset

Details are provided in Supplementary Material, available at *Carcinogenesis* Online.

RNA extraction, cDNA synthesis, RT-PCR and qPCR

Trizol (Invitrogen) based total RNA extraction was achieved from 80% confluent cultures of cell lines following respective treatments as described previously (18). Details are provided in Supplementary Material, available at *Carcinogenesis* Online along with list of primers.

Immunostaining, image acquisition and quantification of signal intensity

Immunostaining was performed as described previously (18). Quantification of signal intensities for transcription factors was performed with the LAS-AF software (Leica Microsystems, Wetzlar, Germany). Briefly, ROIs were defined from phase contrast images around nuclear margins (for TFs) or cell boundaries (for E-cadherin [Cdh1], Vim) of each cell followed by extraction of signal intensities for Hoechst and respective

fluorescent channels. Relative nuclear signal intensity for transcription factors was determined as a ratio of TF-/Hoechst-associated fluorescence, while Cdh1,Vim were normalized to unstained (primary antibody control) samples to eliminate nonspecific signals obtained due to the staining protocol. Quantification was performed for a minimum of 50 nuclei for each sample. List of antibodies used is provided in Supplementary Material, available at *Carcinogenesis* Online.

Immunoblotting

Immunoblotting protocols were followed as described previously (18). List of antibodies used is provided in Supplementary Material, available at *Carcinogenesis* Online.

In vitro wound healing assay, live cell imaging, processing and quantification of data, principal component analysis for migration

Wound healing assay was performed as per previous protocols (14). Under specific experimental conditions media additives were administered including 5% serum, TGFβ (10 ng/ml), BMP7 (10 ng/ml) or a combination of both growth factors. The wound was allowed to heal and was monitored up to 144 h. Images were captured on Olympus IX71 microscope and analyzed by the T-Scratch Software (Tobias Gebäck and Martin Schulz).

For live cell imaging, images were acquired for 30 h, following infliction of wound on a cell monolayer, on an inverted laser scanning confocal fluorescence LPSS5 microscope maintained at 37°C, 5% CO_2 atmosphere (Leica Microsystems). In case of specific treatments, additives were added as described previously. For live cell imaging of paclitaxel-treated cells, drug treatment for 48 h was followed by harvesting of residual cells and seeding for wound healing assay. In the absence of additives, live cell imaging was performed in serum free media in the presence of 20 ng/ml of mitomycin 'C' (Sigma). Images captured for live cell imaging were exported from the LAS AF software (Leica Microsystems) with .avi extensions. For elimination of shadow effects in images.avi files were opened in Fiji software, duplicated, inverted and averaged with original image using the Image Calculator. Processed files were subjected to thresholding to obtain binary images which were eventually processed through MTrack2 plugin to obtain *X* and *Y* coordinates for all the cells detected in the microscopic field of interest. Positional coordinates over a period of 16 h was used to calculate mean displacement and velocity for each cell, however, cells lacking this data at any time point were excluded from further analysis. Furthermore, binary images were processed through the BioVoxxel plugin to determine the mean number of nearest neighbors (Nn) around each cell particle. One cell diameter was used as a threshold to identify Nn around each cell as depicted in Supplementary Figure S2, available at *Carcinogenesis* Online. Mean displacement, velocity and number of Nn were analyzed in matlab2013b (Mathworks) with an open source code available for principal component analysis. First two components capturing maximum variance of the data were represented using SigmaPlot 10.0 software (SPSS).

Boyden chamber invasion assay

Trans-well invasion assays were performed, as described previously (19).

Suspension culture assessment

Suspension cultures for HGSC cell lines were generated as described by earlier studies (20).

FACS sorting and flow cytometry

FACS and Flow cytometry were performed as described previously (20). List of antibodies used is provided in Supplementary Material, available at *Carcinogenesis* Online.

Cloning, expression and purification of GST–Tcf21 protein

Human Tcf21 cDNA was amplified from A4 cells, cloned into pGEX-6P-1 GST vector and transformed into *Escherichia coli* BL21 codon Plus (Agilent Technologies, Santa Clara, CA). Details of cloning and protein purification are provided in Supplementary Materials and Methods, available at *Carcinogenesis* Online.

Electrophoretic mobility shift assay (EMSA)

EMSA was performed as described previously (18).

Chromatin immunoprecipitation assay and ChIP-PCR

ChIP was performed as described earlier (19); ChIPped DNA amplified using the GenomePlex Complete Whole Genome amplification kit as per manufacturer's instructions (Sigma). Specific primers were used to amplify E-boxes within promoter regions of genes, amplified products run on 1.5% agarose gels, and band intensities measured by densitometric analysis using Genetool3.6 (Syngene, Bengaluru, India). List of antibodies and primers used is provided in Supplementary Material, available at *Carcinogenesis* Online.

Luciferase constructs and luciferase assay

Luciferase constructs for E-cadherin and Slug wild-type promoters along with deletion mutants ΔS1–S2 were previously generated in the pGL3 luciferase plasmid (18). All constructs were verified by sequencing. 0.5×10^5 OVCAR3, A4, and derivatives were transfected with 0.5 µg luciferase reporter plasmids control and E-cadherin/Slug promoter containing plasmids in 24-well plates using Lipofectamine 3000 (Invitrogen). Renilla luciferase was added (10 ng) to each transfection as control. Luciferase activity was measured using a Dual Luciferase assay kit (Promega, Madison, WI) either post-transfection with pEGFP–Tcf21 and/or post paclitaxel treatment. Empty pEGFP and pGL3 vectors were used as controls.

Quantitative and statistical analysis

Pearson's correlation coefficient across the TCGA–HGSC datasets was calculated using the GraphPad Prism 6.0 software. Significant differences in gene expression profiles across the HGSC cell line panel were calculated by one-way analysis of variance using the Sigma Stat 3.5 Software. Significant differences following treatments in gene expression profiles, invasive capabilities and wound healing properties of HGSC cell lines and derivative clones, and luciferase activity for promoter assays were calculated by paired Student's *t*-test using the Sigma Stat 3.5 Software. Similarly, ChIP binding efficiencies were calculated by unpaired Student's *t*-test. Differences in nuclear intensities of Tcf21, Slug, Cdh1 and Vim were calculated by Tukey's test using the Sigma Stat 3.5 Software. Differences were considered significant if $P < 0.05$.

Results

Tcf21 and Slug expression governs a multistep phenotypic axis in HGSC

Previous data (14) identified class-specific expression of 13 transcription factors that were examined in the present study for association with distinct phenotypic states in HGSC (TFs; Supplementary Table S1, available at *Carcinogenesis* Online); immunomodulatory TFs AIF1, ETV7 were excluded from further analysis due to limitations of our experimental systems. Promoter occupancies between the remaining TFs, derived from consensus DNA binding sequences, predicted a cross-regulatory network that included 10 TFs from Class 1 (CCM/epithelial tumor class) *viz.*, *Tcf21, Sall2, Peg3, Gata4, Kcnip3, Znf219, Foxl2, Gli1, Sox12, Tcf7l1* and one TF *viz.*, Slug from Class 2 (EMT/mesenchymal tumor class; Figure 1a; Supplementary Figure S1a, available at *Carcinogenesis* Online; details of TF network generation are provided in Supplementary Material, available at *Carcinogenesis* Online) Correlation analysis among these TFs predicted coregulation of *Tcf21, Gata4, Peg3, Gli1, Foxl2* that correlated positively with each other and negatively
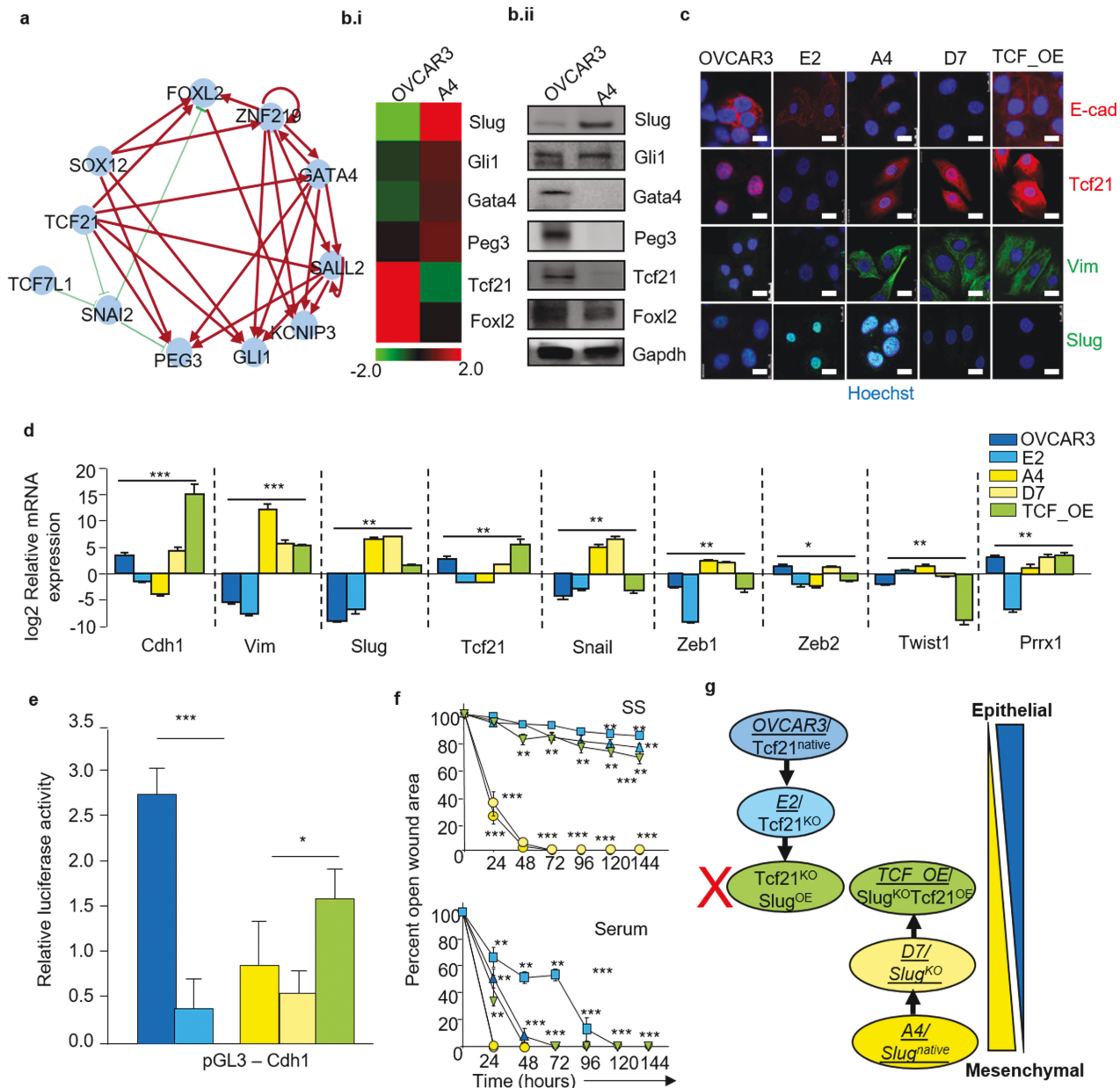
Figure 1. Tcf21 and Slug govern cellular phenotypes in HGSC. (**a**) Predicted transcription factor (TF) network of cross-regulatory activities, red arrows/green bars represent likely activator/repressor functions respectively; (**b**) Expression profiling of *Snai2*(Slug), *Gli1*, *Gata4*, *Peg3*, *Tcf21*, *Foxl2* in OVCAR3 and A4 cells by (i) qPCR (heatmap) and (ii) immunoblotting, GAPDH used as endogenous control. Immunoblots represented in the panel are derived from the same experiment and have been processed in parallel; (**c**) Immunostaining of Tcf21, Slug, Ecad, Vim in parental (OVCAR3/Tcf21native, A4/Slugnative) and derivative cells (E2/Tcf21K/O, D7/SlugK/O and TCF_OE/SlugK/OTcf21OE), nuclei visualized with Hoechst, Scale bars—20 μm; (**d**) Expression profiles of phenotypic markers (*Cdh1, Vim*) and TFs (*Snai2*-Slug, *Tcf21, Snail, Zeb1, Zeb2, Twist1, Prrx1*) in parental (OVCAR3, A4) and derivative (E2, D7, TCF_OE) cells, normalization with GAPDH; (**e**) Reporter assays to determine the E-cadherin promoter activity in derivative clones (E2, D7, TCF_OE) and parental cells (OVCAR3, A4), luciferase activity normalized to native luciferase vector: pGL3; f. Graphical representation of wound healing efficiency of parental (OVCAR3, A4) and derivative cells (E2, D7, TCF_OE), in the absence and presence of serum (upper and lower panels respectively); (**g**) Flow chart depicting an epithelial–mesenchymal (EM) axis along which parental (OVCAR3, A4) and derivative cells (E2, D7, TCF_OE) are placed. Color scheme depicts each of the cell lines represented in preceding panels. All data are representative of experiments performed in triplicate and depicted as mean ± SEM. *$P < 0.05$, **$P < 0.01$, ***$P < 0.001$.

with *Snai2* (Slug) in the TCGA dataset (Supplementary Figure S1b, available at *Carcinogenesis* Online). Profiling these TFs in class-representative cell lines robustly associated CCM-Class (OVCAR3 cells) with Tcf21 and EMT-Class (A4 cells) with Slug expression; however, the lack of a strong correlation between mRNA and protein profiles limited their further validation (Figure 1b; Supplementary Figure S1c, available at *Carcinogenesis* Online). Thus, molecular profiles in our cell line models and

previous association of Tcf21, Slug with the epithelial, mesenchymal phenotypes, respectively (19,21), prompted our focused efforts on discerning their role in cellular plasticity of ovarian cancer cell lines.

Toward ascertaining the role of Tcf21 and Slug in phenotype maintenance, we further derived knockout (K/O) clones of the dominant TF (genomic editing by commercial CrispR constructs) followed by overexpression (OE) of the other TF in parental cell

lines—OVCAR3 (Tcf21^native) and A4 (Slug^native; Supplementary Figure S1d, available at *Carcinogenesis* Online); stable knockouts were affirmed by sequencing (data not shown). Molecular profiles revealed high Tcf21, E-cadherin (*Cdh1*) expression in OVCAR3 cells whereas Tcf21^K/O(E2) exhibited high nuclear Slug and low *Cdh1*. A4 cells expressed high Slug, Vimentin (*Vim*) with low *Cdh1*, however, sustained expression of other EMT–TFs (Zeb1/2, Twist1, Snail, Prrx1) in the Slug^K/O (D7) led to minimally altered *Cdh1* and *Vim* despite enhanced nuclear Tcf21 localization (Figures 1c and d). Interestingly, A4_Slug^K/OTcf21^OE (TCF_OE) cells exhibited reduced expression of EMT–TFs and correlated with enhanced *Cdh1* while retaining *Vim* expression (Figures 1c and d). High luciferase activity in OVCAR3 and TCF_OE cells (reporter assay for *Cdh1* promoter harboring Slug binding E-box sequences), and reduced activity in E2, A4 and D7 cells suggested phenotypic variability as a function of Tcf21 and Slug expression (Figure 1e). Functional validation identified differential rates of wound closure between parental and derivative clones to be positively influenced by serum (Figure 1f). In the absence of serum, OVCAR3 and E2 cells failed to induce wound closure, suggesting the absence of functional EMT despite enhanced *Slug* and reduced *Cdh1* levels in E2 cells; wound healing efficacy was drastically curbed in TCF_OE as compared with A4 and D7 cells. Derivative clones, thus represented intermediate phenotypes along the EM axis wherein OVCAR3 (Tcf21^native) and E2 (Tcf21^K/O) exhibited a rigidity toward functional phenotypic alteration as compared with A4 (Slug^native), D7 (Slug^K/O) and TCF_OE (Slug^K/OTcf21^OE) cells as indicated by molecular and functional readouts (Figure 1g). These findings while associating Tcf21, Slug with epithelial, mesenchymal phenotypes, respectively, highlight the inability of these TFs toward inducing a bilateral phenotypic switch and possibly imply EM transitions as a multistep process.

Tcf21–Slug status of HGSC cells associates with differential modes of migration

A disconnect between wound closure efficacies and expression of phenotypic markers in derivative clones prompted the adoption of high-resolution approaches to investigate their respective migratory modalities. Time lapse microscopy imaging improved the *in vitro* wound healing assay by enhancing the visual output. OVCAR3 and E2 cells exhibited proliferation-driven cell displacement that we termed passive CCM (pCCM), A4 mediated rapid wound healing through a combination of single cell and active CCM (EMT and aCCM, respectively) while its derivatives D7, (Slug^K/OTcf21^OE) exhibited aCCM exclusively (Supplementary Video S1, available at *Carcinogenesis* Online). Cell position coordinates during wound closure allowed quantification of these processes by virtue of migration trajectories, mean cell velocity and Nn (Supplementary Figure S2, available at *Carcinogenesis* Online). pCCM driven wound closure was associated with minimal cell displacement, low migratory velocity and a high Nn; aCCM was defined by moderate displacement/velocity and high Nn while EMT cells exhibited high displacement/velocity with low Nn (Figure 2a–c). Serum addition enhanced displacement, velocity and reduced Nn in aCCM and EMT phenotypes while pCCM cells increased Nn by virtue of extensive cell proliferation. Presence of mitomycin 'C', a proliferation inhibitor, in the absence of serum distinguished cell displacement attributed by active migration (aCCM/EMT) as opposed to cell division driven passive movement (pCCM). Principal component analysis performed with these datasets supported differential migratory modes wherein PC1 (variance between velocity and displacement versus Nn) and PC2 (variance between displacement

versus velocity) effectively resolved cell lines associated with pCCM, aCCM and EMT–aCCM modes of migration while capturing serum induced shifts in respective modalities (Figure 2d). Differential Nn frequencies between A4 and D7 proved a useful metric for distinguishing EMT from aCCM apart from the visualization in real time imaging. While visual outputs affirmed association of Tcf21 and Slug with distinct migratory modes in the derivative clones, principal component analysis permitted an unbiased segregation of these modalities as a function of TF expression. This gradient of migration modalities effectively agrees with the artificial E to M spectrum depicted in Figure 1g, emphasizing rigidity of the E phenotype, and supporting the absence of biphasic phenotypic switches in HGSC.

Tcf21 is a transcriptional repressor of Slug

In view of the predictive TF network and inverse associations in our derivative clones, we probed possible cross-regulation between Tcf21 and Slug. Luciferase activity (reporter assay for *SNAI2* promoter harboring Tcf21-binding consensus E-box sequences) was severely reduced in A4 cells exogenously overexpressing Tcf21 (Figure 3a and b). *In vitro* binding assays also affirmed physical interactions between recombinant Tcf21 and S1, S3, S5 *SNAI2* E-boxes. Further probing of Tcf21-bound chromatin complexes in OVCAR3 cells through immunoprecipitation indicated affinity for S2, S3, S6 *SNAI2* E-boxes (Figure 3c and d). Similar regulation of Tcf21 expression by Slug was not observed. Varied Tcf21 binding affinities in cell-free and cell-based systems emphasize the significance of cellular context in target recognition and imply possible involvement of other coregulatory factors in the process. These findings suggest transcriptional repression of Slug by Tcf21 toward maintenance of epithelial properties in HGSC.

HGSC tumors and cell lines intrinsically display a spectrum of phenotypes and modes of migration

Toward resolution of distinct phenotypes in HGSC at steady state and describing EM transitions as a multistep process, we primarily analyzed the heterogeneity of phenotypic markers in TCGA–HGSC dataset. Correlation analysis of gene expression data for epithelial and mesenchymal markers generated four clusters (C1–C4) representative of specific phenotypic attributes (Supplementary Figure S3a, available at *Carcinogenesis* Online). C1 genes included components of epithelial cell junctions and keratins, C2 genes associated with mesothelial and myoepithelial phenotypes across several tissues (breast, ovary, peritoneal linings) (22–24), C3 comprised of cell junction molecules encountered in mesenchymal cells (10), while C4 included genes commonly expressed in the endothelial and stromal lineages (25,26). Apart from segregation of these gene groups, correlation analysis identified a heterogeneity of phenotypic markers in HGSC which could be indicative of existing diverse phenotypes. Hierarchical clustering of known epithelial and mesenchymal TFs in this data yielded five distinct tumor groups (Supplementary Figure S3b, available at *Carcinogenesis* Online). Two of these were exclusively epithelial (E) and mesenchymal (M) while a third was considered EM by virtue of a heterogeneous double-positive signature. A separate cluster identified as intermediate E (iE), expressed E markers, Snail, Twist1 but lacked Tcf21, while the tumor group with low EMT–TF expression was assigned as iM.

In vitro validation of identified phenotypic states proceeded *via* parallel screening of E, M markers and TF transcripts across a panel of HGSC cell lines. Molecular profiles
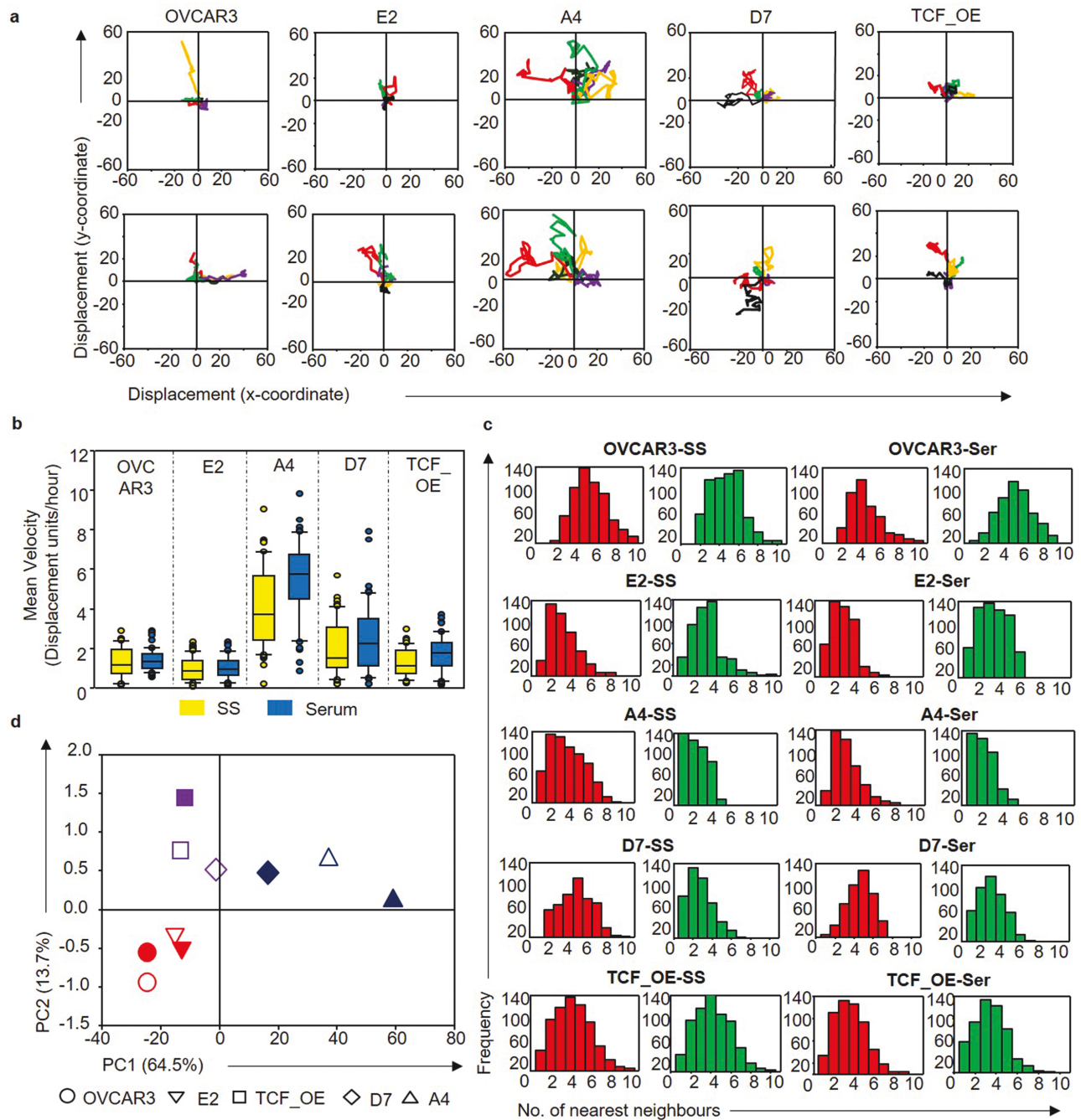
Figure 2. Quantitative metrics for resolution of migratory modalities. (**a**) Trajectories depicting migration directionality for parental cell lines (OVCAR3/Tcf21[native], A4/Slug[native]) and respective derivatives (E2/Tcf21[K/O], D7/Slug[K/O] and TCF_OE/Slug[K/O]Tcf21[OE]). Plots represent trajectories of five randomly selected cells; (**b**) Representative plots depicting mean migratory velocity of parental (OVCAR3, A4) and derivative cells (E2, D7, TCF_OE). Displacement and velocity were derived from 'x' and 'y' positional coordinates detected over a 16 h duration; (**c**) Frequency of Nn for parental cell lines (OVCAR3, A4) and derivative clones (E2, D7, TCF_OE) at 0 h (red) and 16 h (green) time points distribution graphs depict Nn data for 750 cells. Experiments were performed in the absence/presence of serum. All cells identified in the microscopic field as particles were analyzed for displacement, velocity and Nn. However, only data points inclusive of the 'X', 'Y' coordinates and Nn over the entire duration of 16 h were used for data representation and interpretation; (**d**) Principle component (PC) analysis of time-lapse imaging-based migration data of parental (OVCAR3, A4) and derivative cells (E2, D7, TCF_OE), PC1—variance between displacement (final Y) and velocity versus Nn, PC2—variance between displacement and velocity; color gradient depicts migratory modes, blue-EMT, purple-aCCM, red-pCCM; filled and empty shapes indicate presence and absence of serum, respectively.

resolved five phenotypic states through definitive correlations between E (Cdh1,Ck19), M (Vim,FAP) markers and TFs (Tcf21, Slug and Prrx1 isoforms 1a and 1b; Supplementary Figure S3c–e, available at *Carcinogenesis* Online; Prrx1a, Prrx1b transcripts—P1a, P1b, respectively, protein represented as

Prrx1) (27). Nonavailability of isoform-specific Prrx1 antibodies restricted further definitive studies for this TF. OVCAR3, OVCA432 (high E, nuclear Tcf21, low P1a–P1b–nuclear Prrx1, low nuclear Slug) and OVMZ6 cells with an inverse profile defined the E and M ends of the spectrum. CAOV3 and
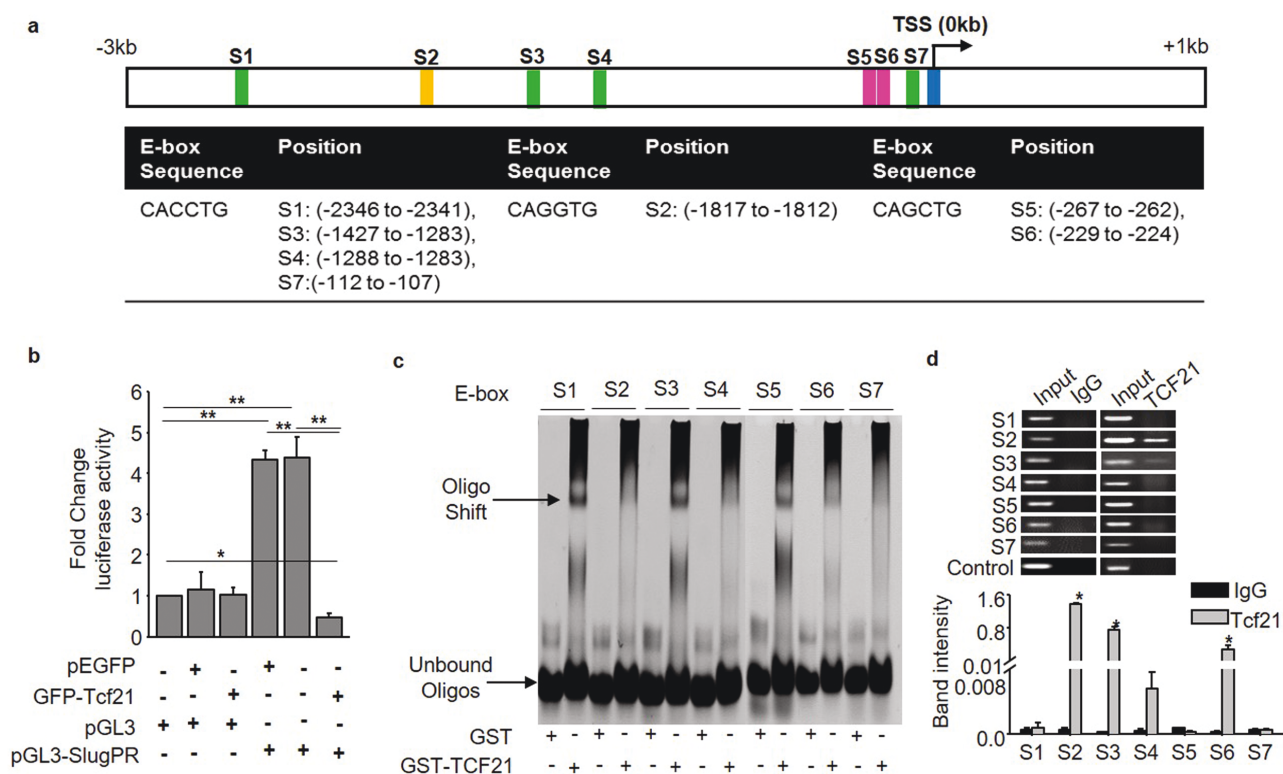
Figure 3. Tcf21-mediated Slug repression by direct promoter binding. (**a**) Schematic representation of Slug promoter region depicting the location and sequences of E-boxes. Promoter region: −3 kb to + 1 kb from transcription start site (TSS); (**b**) Reporter assays to determine effects of Tcf21 on wild type Slug promoter in A4 cells, luciferase activity normalized to untransfected cells; pEGFP: empty GFP vector, GFP–Tcf21: Tcf21–pEGFPC1 recombinant vector, pGL3: native luciferase vector, pGL3–SlugPR: pGL3 containing Slug promoter; (**c**) Representative EMSA of GST–Tcf21 recombinant protein binding to E-boxes in Slug promoter region in a cell free system, GST protein used as control; (**d**) ChIP–PCR analysis of Tcf21 binding to E-box elements in Slug promoter in OVCAR3 cells, IgG used as isotype control, cross-linked fragmented DNA considered as Input. All data are representative of experiments performed in triplicate and depicted as mean ± SEM. $^*P < 0.05$, $^{**}P < 0.01$, $^{***}P < 0.001$.

OV90 were identified as iE (high E, FAP, nuclear Tcf21, low P1a–P1b-moderate nuclear Prrx1, low nuclear Slug), OVCA420 and PEO14 as EM (E, M markers, all TFs in nucleus) and A4 as iM phenotype (CK19, M markers, low cytoplasmic Tcf21, high P1b, nuclear Prrx1 and Slug). These phenotypes could be perturbed by external stress such as serum deprivation that induced Cdh1 and nuclear Tcf21 expression, concomitantly decreasing Slug, FAP and Vim in the cell line panel to shift the spectrum toward the E phenotype (Figure 4a and b).

Probing phenotypic–functional associations assigned spheroid generation capabilities to intermediate states while E and M cells formed clumps/aggregates (Figure 4c). Except the E state, all cell lines were highly invasive in response to a serum gradient (Figure 4d). Differential migration capabilities were evident wherein A4, OV90 and OVCA420 cells filled the open wound area in absence of serum as opposed to E/iE and surprisingly M cells that required serum to achieve wound closure (Figures 4e.i and e.ii). Live imaging and PC analyses based on predefined quantitative metrics revealed pCCM in E and iE, aCCM in EM, coupling of aCCM–EMT in iM and EMT in M cells (Supplementary Video 2, available at *Carcinogenesis* Online; Figure 4e.iii). Interestingly, serum deprivation led to nuclear localization of Slug in a few EM state cells that possibly induces rare EMT events visualized in live imaging. Thus, the cell line panel reaffirmed existence of a phenotypic spectrum in HGSC defined by inherent Tcf21–Slug profiles and captured cellular plasticity as intermediate states following growth factor deprivation.

Microenvironment influenced phenotypic interconversions are captured by nuclear Tcf21 and Slug expression

Further examination of cellular plasticity across the EM axis and phenotype specific association of Tcf21–Slug, proceeded with exposure of the cell line panel and derivative clones to growth factors known to mediate directed phenotypic changes. TGFβ–BMP signaling plays a crucial role during ovarian/fallopian tube development and homeostasis. Additionally, the antagonistic influence of TGFβ1 and BMP7 on epithelial and mesenchymal phenotypes make them suitable triggers to assess HGSC cell line plasticity. E and iE cells were refractory in their response to both growth factors; BMP7 induced Cdh1, nuclear Tcf21 and reduced Slug levels whereas TGFβ1 exposure upregulated Slug concomitantly with reduced Cdh1 and Tcf21 in EM, iM and M cells (Figure 5a; Supplementary Figures S4a, S5a, and S6, available at *Carcinogenesis* Online). Dominant effects of BMP7 over TGFβ1 were observed in EM and iM cell lines (high Cdh1, nuclear Tcf21, low Slug) when the growth factors were provided in combination. Similarly, exposure of derivative clones (E2, D7 and TCF_OE) and parental cell lines (OVCAR3, A4) generated distinct responses that correlated with an inherent Tcf21–Slug balance. OVCAR3 cells were refractory to both growth factors while E2 responded poorly to BMP7 and exhibited enhanced nuclear Slug expression following exposure to TGFβ1. A4, D7, TCF_OE cells responded to BMP7 through nuclear localization of Tcf21, enhanced Cdh1 expression and reduced Slug. Conversely, TGFβ1 repressed Tcf21, Cdh1 in A4 and D7 cells with concomitant increase in Slug and Vim expression while TCF_OE
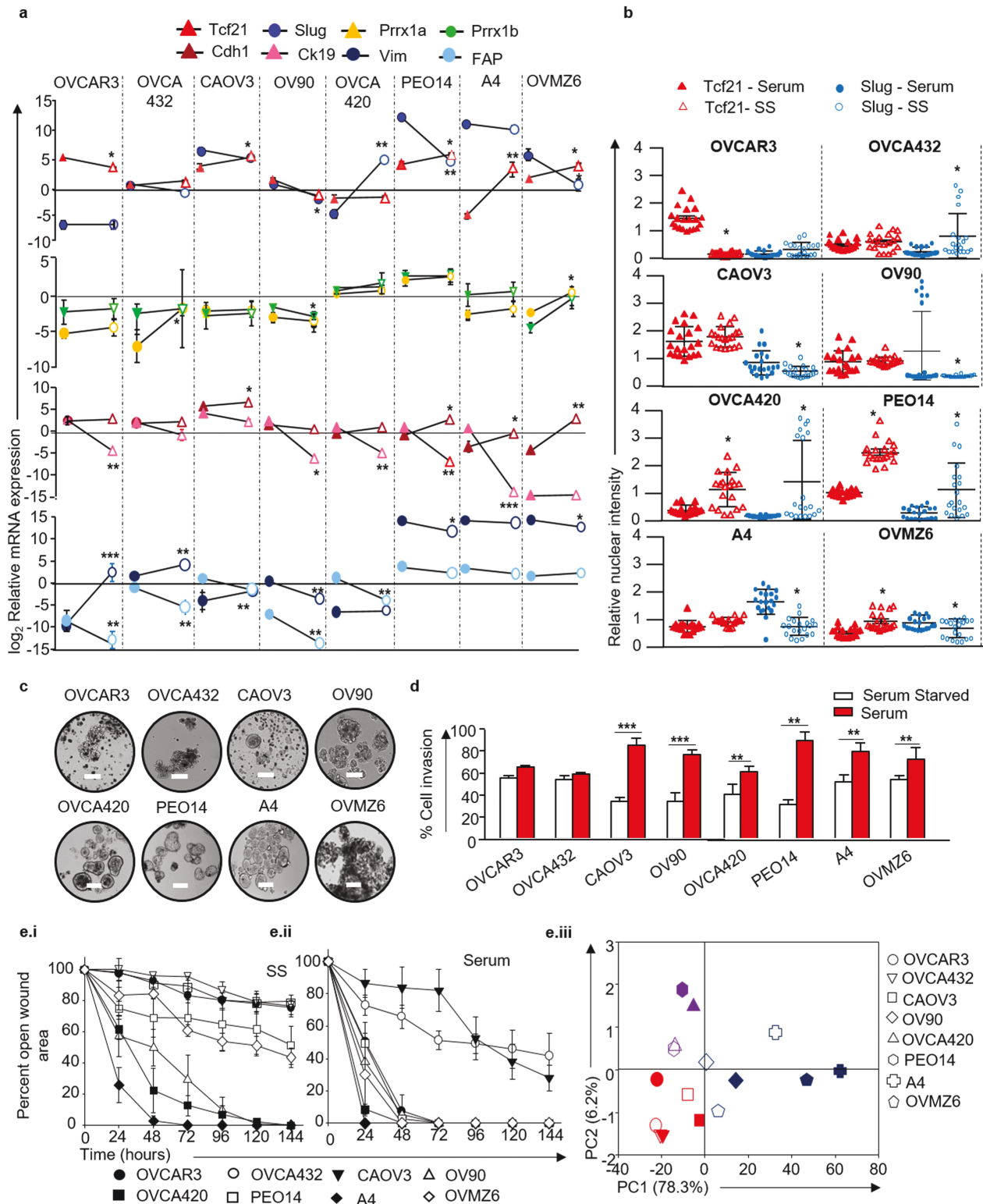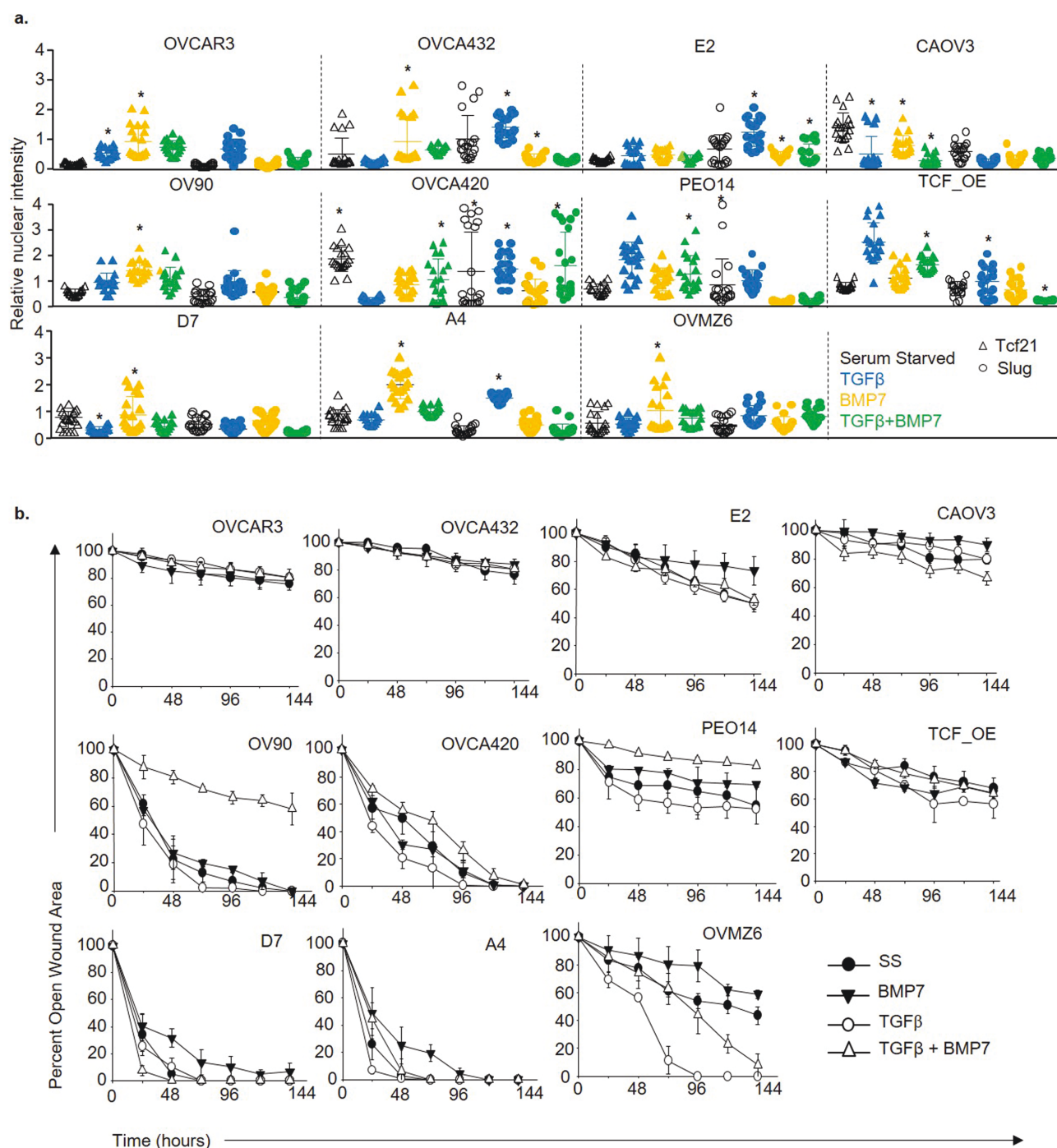
Figure 4. Resolution of the epithelial-mesenchymal phenotypic axis highlights differential functionalities as a function of Tcf21 and Slug localization. (**a**) Expression profiles of Tcf21, Slug, Prrx1 isoforms, Cdh1, Ck19, Vim and FAP in HGSC cell lines at steady states and post serum deprivation normalized with GAPDH. Filled shapes indicate the presence of serum and empty shapes indicate that cells were serum starved; (**b**) Representative graphs depicting frequency and intensity of Tcf21 and Slug positive nuclei in HGSC cell lines. Data depicts fluorescence intensities for each transcription factor measured across five random microscopic fields and quantified relative to the signal for Hoechst; (**c**) Representative images of suspension culture morphology (scale bars—200 μm); (**d**) Percent cell invasion in Boyden chamber matrigel assay in the absence and presence of serum; (**e**) Efficacy of wound healing in the (i) absence and (ii) presence of serum; (iii) Principle component analysis used to project segregation of migratory modes in the phenotypic spectrum based on quantitative metrics—final 'Y', velocity and Nn—emerging from time-lapse based migration data; color gradient represents the migratory modes of each cell line blue-EMT, purple-aCCM, red-pCCM; filled shapes indicate the presence of serum and empty shapes indicate that cells were serum starved. All data are representative of experiments performed in triplicate and are depicted as mean + SEM, *$P < 0.05$, **$P < 0.01$, ***$P < 0.001$.

Figure 5. Tcf21/Slug subcellular localization correlates with HGSC wound healing efficacy. (a) Representative graphs depicting frequency and intensity of Tcf21 and Slug positive nuclei in HGSC cell lines and derivative clones (E2/Tcf21^K/O, D7/Slug^K/O and TCF_OE/Slug^K/O^Tcf21^OE) exposed to BMP7, TGFβ and BMP7 + TGFβ. Data depicts fluorescence intensities for each transcription factor measured across five random microscopic fields and quantified relative to the signal for Hoechst; (b) Graphical representation of wound healing efficiency of HGSC cell lines and derivative clones (E2, D7 and TCF_OE) following growth factor treatment as indicated; All data are representative of experiments performed in triplicate and depicted as mean ± SEM. *P < 0.05, **P < 0.01, ***P < 0.001.

responded poorly to the same (Figure 5a; Supplementary Figures S4b, S5b, and S6, available at *Carcinogenesis* Online). Thus, clone responses to combination of these two growth factors agreed with observations in the cell line panel. Integrating Tcf21 and Slug transcript profiles across all cell lines and derivatives under varying culture conditions (steady-state, serum-deprivation, growth factor exposure) with TF-promoter binding studies aided

the generation of a mathematical model that identified TCF21^high–SLUG^low (E), TCF21^low–SLUG^high (M) and Tcf21^mod–Slug^mod (EM) as stable phenotypes while iE and iM were depicted as metastable states associated with phenotypic switches. Drastic fluctuations in Tcf21 and Slug expression correlated with transitions at the E and M ends, respectively (Supplementary Figure S4c, available at *Carcinogenesis* Online).

Functional evaluation of the microenvironmental influences revealed rate of wound closure to be restricted by BMP7 and enhanced by TGFβ in EM, iM and M, while minimal changes were evident in E and iE cells (Figure 5b). Combination treatment with both cytokines revealed a dominant effect of BMP7 over TGFβ in hindering wound closure. This functionality was altered in derivative clones wherein E2 exhibited moderately enhanced wound closure following exposure to TGFβ with minimal response to BMP7 in agreement with altered Tcf21–Slug balance; TGFβ enhanced and BMP7 reduced wound closure in D7 cells whereas TCF_OE exhibited minimal alterations. These observations assign cellular rigidity to E, M and plasticity to intermediate states. Conclusively, Tcf21–Slug expression and subcellular localization correlates with cellular states across the spectrum and are possible determinants of functionality in migration and phenotypic plasticity.

Drug-induced plasticity in HGSC associates with Tcf21–Slug crosstalk

Phenotypic plasticity in the EM spectrum was further assessed in response to a chemotherapeutic challenge (paclitaxel) and evaluated as a function of Tcf21–Slug expression. PC analysis of live migration derived metrics identified a switch from EMT to aCCM mode for M and iM cells after treatment (maximum variance along both PCs), EM and iE adhered to their characteristic modes of migration albeit at reduced velocities (moderate variance along both PCs) while pCCM phenotype in E cells was unaltered (Figure 6a; Supplementary Video S3, available at *Carcinogenesis* Online). These altered migratory metrics across the spectrum were associated with increased nuclear Tcf21 concurrently with reduced Slug expression (Figure 6b). Pacliaxel exposure induced an iE phenotype in E and iE cell lines, a similar shift toward the E phenotype was evident in EM, iM and M cells although the extent of each shift was distinct. To assign a mechanistic understanding to drug-induced phenotype switching, we probed occupancy of Tcf21 at the Slug promoter as a read-out of the E phenotype. Enhanced affinity of Tcf21 for the S2, S3 E-boxes in *SNAI2* promoter was identified following paclitaxel treatment and further complemented by negligent luciferase activity in Tcf21 overexpressing paclitaxel treated A4 cells (Figure 6c and d). Deletion of S2 E-box from the Slug promoter dramatically curbed Tcf21 mediated Slug
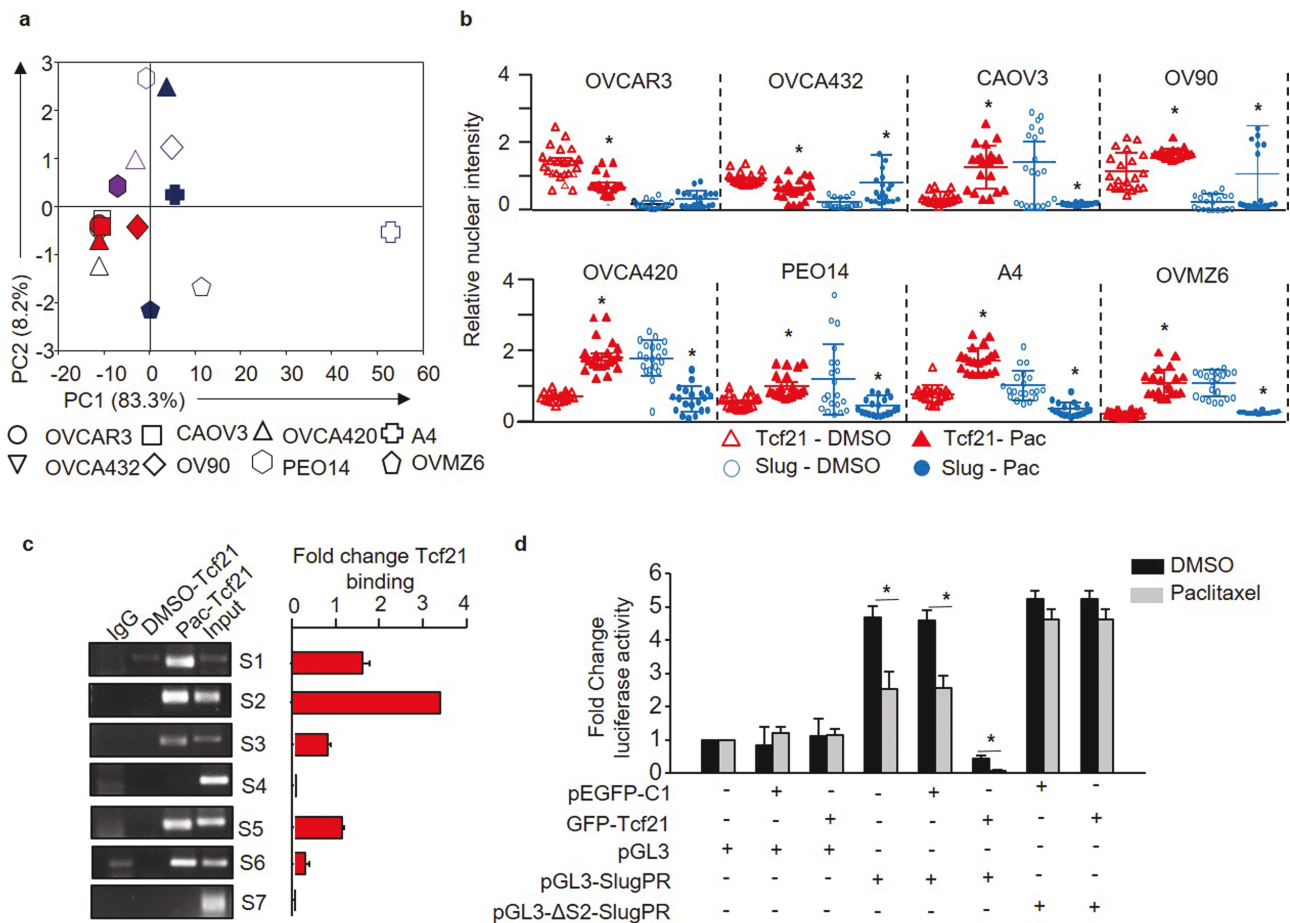

Figure 6. Class-switching in HGSC correlates with therapy induced Slug repression via Tcf21. a PC analysis used to project migratory modes of the different HGSC cell lines following paclitaxel exposure, PC1 and PC2 as described earlier; empty and filled shapes correspond to 0.1% DMSO and paclitaxel exposure, respectively in subsequent figures; (b) Representative graphs depicting frequency and intensity of Tcf21 and Slug positive nuclei in HGSC cell lines, data depicts fluorescence intensities for each transcription factor measured across five random microscopic fields following exposure to 0.1% DMSO (vector control)/paclitaxel (Pac) and quantified relative to the signal for Hoechst; (c) ChIP-PCR analysis depicting enrichment of Slug promoter regions in Tcf21 pulldown following paclitaxel exposure of A4 cells. IgG and DMSO used as isotype and vector control, respectively; (d) Reporter assays to determine effects of Tcf21 on wild type Slug promoter in A4 cells, luciferase activity normalized to untransfected cells. pEGFP: empty GFP vector, GFP–Tcf21: Tcf21–pEGFPC1 recombinant vector, pGL3: native luciferase vector, pGL3–SlugPR: pGL3 containing Slug promoter, pGL3–ΔS2–SlugPR: pGL3 containing Slug promoter with deleted S2 E-box. All data are representative of experiments performed in triplicate and are depicted as mean ± SEM. *$P < 0.05$, **$P < 0.01$, ***$P < 0.001$.

repression in the luciferase assay. These results together identify a Tcf21-driven phenotypic switch in HGSC cells that results in the emergence of epithelial traits.

Discussion

The anatomical proximity of ovarian surface and FT epithelium as sites of perturbed epithelial integrity, following ovulation and wound healing, have led to conflicting opinions on the cell-of-origin of ovarian cancer (14,28,29). The present study, restricted to the most aggressive subtype *viz.* HGSC, identifies Tcf21–Slug cross-talk in maintenance of intrinsic cellular states, wherein Tcf21-mediated Slug repression emerged as a feature of the epithelial phenotype. While previous studies exclusively implicate Slug as an EMT–TF (30), Tcf21 exhibits a tissue-specific activity in facilitating EM transitions. In the context of cardiac development, Tcf21 expression is linked with the onset of EMT in endocardial progenitors toward sculpting of the cardiac cushion and valves (31). Conversely, repression of this TF in renal and lung carcinomas results in overt metastasis, which can be suppressed through the activation of Kiss1, a tumor suppressor gene and target of Tcf21 (32,33). A balance of these TFs was associated with cellular plasticity as gauged by molecular and functional responses to extrinsic stimuli. Cells with native Tcf21 were conferred a highly rigid epithelial phenotype whereas dual nuclear positivity (Tcf21 and Slug) was associated with enhanced plasticity. Rigidity of epithelial and mesenchymal states was challenged by deriving intermediates (iE, EM, iM) and correlating phenotypes with discrete modes of migration despite comparable invasion (Supplementary Figure S7a, available at *Carcinogenesis* Online). The latter is thus underscored as a universal feature in HGSC and uncoupled from EMT (34).

Differential migration recapitulates events at the tumor edge (35,36), wherein destabilization of the tissue architecture by a degradative secretome and altered mileu may promote EMT, while exertion of tensile forces by adherens junction-linked acto-myosin complexes may induce CCM allowing invasion/deposition of tumor cells in the peritoneum (37–42). Our quantification of *in vitro* metrics, distinguished discrete migratory modalities across the phenotypic spectrum and correlated them with Tcf21–Slug expression. Application of live cell imaging also enhanced resolution of the *in vitro* wound healing assay, thus generating an improved informative method. Exploring the physiologically relevant BMP7–TGFβ signaling dynamics during ovulation (43–45), we identified the imposition of reduced migration with induction of nuclear Tcf21 and epithelial features through BMP7 exposure, while TGF-β enhanced EMT/aCCM mediated migration and mesenchymal features triggered by Slug expression (Supplementary Figure S7b, available at *Carcinogenesis* Online). While TGFβ has been extensively associated with HGSC pathology (46,47), previous reports on BMP7 have indirectly implied its role in therapy resistance, tumor progression and inhibition of TGFβ signaling in ovarian cancer (48–50). However, our findings conclusively identify a reciprocal role for these cytokines in governing cellular plasticity of ovarian cancer cells, which is reminiscent of their physiological activity during ovulation (45). These findings may be extrapolated to derive similarities between EMT–aCCM cooperation and OSE wound healing, while maintenance of the rigid, disparate epithelial state during pCCM could be akin to the FT-p53 signature-associated precursor lesions (51,52). Serum withdrawal as well as paclitaxel exposure promoted a Tcf21 driven epithelial state and induced aCCM that could represent a prosurvival mode of cooperative drug resistance. Moreover, Tcf21 expression associated with reduced sensitivity, and in return higher IC_{50}, of HGSC cell to the drug when tested across the HGSC panel (data not shown). Paclitaxel-induced shifts were further associated with Slug repression *via* direct promoter binding by the Tcf21. Interestingly,

while the S2 E-box was most crucial for Slug inhibition, occupancy of multiple E-box sequences by Tcf21 may achieve a greater degree of inhibition. Previous studies on Slug auto-activation identified binding of the EMT–TF to the S2 E-box; thereby promoter occupancy by Tcf21 may prevent Slug–S2 interaction (18). Further support to these observations is provided by the de-repression of Slug promoter following S2 E-box deletion.

Although previous reports implicate Tcf21 as a tumor suppressor gene (53), our findings associate nuclear expression of this TF with therapy resistant populations and emphasize a tissue specific activity. Lack of linear correlations between mRNA and protein expression of these TFs along with dynamic alterations in subcellular localization highlight immense complexity of the Tcf21–Slug axis and warrant further studies pertaining to additional regulatory networks. Our findings also pose imminent questions regarding the epigenetic landscapes of the EM spectrum with respect to this axis; cellular compartment specific interacting partners of these TFs that assist their activity; mechanisms linking Tcf21–Slug to specific migratory modes; biochemical evaluation of protein domains responsible for differential subcellular localization, TF activity, and so on. A retrospective preclinical study from our group has further established Tcf21–Slug as potential biomarkers for HGSC tumor stratification and implied the adoption of tumor class-specific therapeutic regimes to effectively target the disease (54). Our report, thus supports this study and presents Tcf21–Slug as a crucial axis in HGSC cellular plasticity with genuine clinical implications.

Supplementary material

Supplementary data are available at *Carcinogenesis* online.

Data availability

The authors declare that all relevant data supporting findings in this study are available within the article and its supplementary files. Data for quantitative metrics generated from live cell imaging data are available on request.
Conflict of Interest Statement: None declared.

References

1. Watson, C.J. *et al.* (2008) Mammary development in the embryo and adult: a journey of morphogenesis and commitment. *Development*, 135, 995–1003.

2. van Amerongen, R. *et al.* (2012) Developmental stage and time dictate the fate of Wnt/β-catenin-responsive stem cells in the mammary gland. *Cell Stem Cell*, 11, 387–400.

3. Gonzales, K.A.U. *et al.* (2017) Skin and its regenerative powers: an alliance between stem cells and their niche. *Dev. Cell*, 43, 387–401.

4. Proia, T.A. *et al.* (2011) Genetic predisposition directs breast cancer phenotype by dictating progenitor cell fate. *Cell Stem Cell*, 8, 149–163.

5. Guo, W. *et al.* (2012) Slug and Sox9 cooperatively determine the mammary stem cell state. *Cell*, 148, 1015–1028.

6. Varga, J. *et al.* (2017) Cell plasticity in epithelial homeostasis and tumorigenesis. *Nat. Cell Biol.*, 19, 1133–1141.

7. Nieto, M.A. *et al.* (2016) EMT: 2016. *Cell*, 166, 21–45.

8. Tan, T.Z. *et al.* (2013) Functional genomics identifies five distinct molecular subtypes with clinical relevance and pathways for growth control in epithelial ovarian cancer. *EMBO Mol. Med.*, 5, 983–998.

9. Huang, R.Y. *et al.* (2013) An EMT spectrum defines an anoikis-resistant and spheroidogenic intermediate mesenchymal state that is sensitive to e-cadherin restoration by a src-kinase inhibitor, saracatinib (AZD0530). *Cell Death Dis.*, 4, e915.

10. Tothill, R.W. *et al.*; Australian Ovarian Cancer Study Group. (2008) Novel molecular subtypes of serous and endometrioid ovarian cancer linked to clinical outcome. *Clin. Cancer Res.*, 14, 5198–5208.

11. Bell, D. *et al.* (2011) Integrated genomic analyses of ovarian carcinoma. *Nature*, 474, 609–615.

12. Yang, D. *et al.* (2013) Integrated analyses identify a master microRNA regulatory network for the mesenchymal subtype in serous ovarian cancer. *Cancer Cell*, 23, 186–199.

13. Kanchi, K.L. *et al.* (2014) Integrated analysis of germline and somatic variants in ovarian cancer. *Nat. Commun.*, 5, 3156.

14. Gardi, N.L. *et al.* (2014) Discrete molecular classes of ovarian cancer suggestive of unique mechanisms of transformation and metastases. *Clin. Cancer Res.*, 20, 87–99.

15. Domcke, S. *et al.* (2013) Evaluating cell lines as tumour models by comparison of genomic profiles. *Nat. Commun.*, 4, 2126.

16. Beaufort, C.M. *et al.* (2014) Ovarian cancer cell line panel (OCCP): clinical importance of *in vitro* morphological subtypes. *PLoS One*, 9, e103988.

17. Bapat, S.A. *et al.* (2005) Stem and progenitor-like cells contribute to the aggressive behavior of human epithelial ovarian cancer. *Cancer Res.*, 65, 3025–3029.

18. Kumar, B. *et al.* (2015) Auto-regulation of Slug mediates its activity during epithelial to mesenchymal transition. *Biochim. Biophys. Acta*, 1849, 1209–1218.

19. Kurrey, N.K. *et al.* (2009) Snail and slug mediate radioresistance and chemoresistance by antagonizing p53-mediated apoptosis and acquiring a stem-like phenotype in ovarian cancer cells. *Stem Cells*, 27, 2059–2068.

20. Naik, R.R. *et al.* (2016) A tumor deconstruction platform identifies definitive end points in the evaluation of drug responses. *Oncogene*, 35, 727–737.

21. Chen, Y. *et al.* (2018) Expression of transcription factor 21 (TCF21) and upregulation its level inhibits invasion and metastasis in esophageal squamous cell Carcinoma. *Med. Sci. Monit.*, 24, 4128–4136.

22. Mendez, M.G. *et al.* (2010) Vimentin induces changes in cell shape, motility, and adhesion during the epithelial to mesenchymal transition. *FASEB J.*, 24, 1838–1851.

23. Abid, M.R. *et al.* (2007) NADPH oxidase activity selectively modulates vascular endothelial growth factor signaling pathways. *J. Biol. Chem.*, 282, 35373–35385.

24. Roberts, E.W. *et al.* (2013) Depletion of stromal cells expressing fibroblast activation protein-α from skeletal muscle and bone marrow results in cachexia and anemia. *J. Exp. Med.*, 210, 1137–1151.

25. Hennessy, B.T. *et al.* (2009) Characterization of a naturally occurring breast cancer subset enriched in epithelial-to-mesenchymal transition and stem cell characteristics. *Cancer Res.*, 69, 4116–4124.

26. Rodler, D. *et al.* (2013) Expression of intermediate filaments in the Balbiani body and ovarian follicular wall of the Japanese quail (*Coturnix japonica*). *Cells. Tissues. Organs*, 197, 298–311.

27. Takano, S. *et al.* (2016) Prrx1 isoform switching regulates pancreatic cancer invasion and metastatic colonization. *Genes Dev.*, 30, 233–247.

28. Auersperg, N. (2013) Ovarian surface epithelium as a source of ovarian cancers: unwarranted speculation or evidence-based hypothesis? *Gynecol. Oncol.*, 130, 246–251.

29. Klotz, D.M. (2017) Cells of origin of ovarian cancer: ovarian surface epithelium or fallopian tube? *Arch. Gynecol. Obstet.*, 296, 1055–1062.

30. Gasparics, Á. *et al.* (2018) MRTFs- master regulators of EMT. *Dev. Dyn.*, 247, 396–404.

31. Acharya, A. *et al.* (2012) The bHLH transcription factor Tcf21 is required for lineage-specific EMT of cardiac fibroblast progenitors. *Development*, 139, 2139–2149.

32. Arab, K. *et al.* (2011) Epigenetic deregulation of TCF21 inhibits metastasis suppressor KISS1 in metastatic melanoma. *Carcinogenesis*, 32, 1467–1473.

33. Gooskens, S.L. *et al.* (2018) TCF21 hypermethylation regulates renal tumor cell clonogenic proliferation and migration. *Mol. Oncol.*, 12, 166–179.

34. Schaeffer, D. *et al.* (2014) Cellular migration and invasion uncoupled: increased migration is not an inexorable consequence of epithelial-to-mesenchymal transition. *Mol. Cell. Biol.*, 34, 3486–3499.

35. Klymenko, Y. *et al.* (2017) Heterogeneous cadherin expression and multicellular aggregate dynamics in ovarian cancer dissemination. *Neoplasia*, 19, 549–563.

36. Symowicz, J. *et al.* (2007) Engagement of collagen-binding integrins promotes matrix metalloproteinase-9-dependent E-cadherin ectodomain shedding in ovarian carcinoma cells. *Cancer Res.*, 67, 2030–2039.

37. Mitchell, C.B. *et al.* (2016) Cooperative cell invasion: matrix metalloproteinase-mediated incorporation between cells. *Mol. Biol. Cell*, 27, 3284–3292.

38. Kamble, S.C. *et al.* (2013) Stem cell and cancer stem cell games on the ECM field. *J. Cancer Stem Cell Res.*, 1, 1.

39. Sunyer, R. *et al.* (2016) Collective cell durotaxis emerges from long-range intercellular force transmission. *Science*, 353, 1157–1161.

40. Iwanicki, M.P. *et al.* (2011) Ovarian cancer spheroids use myosin-generated force to clear the mesothelium. *Cancer Discov.*, 1, 144–157.

41. Dong, Y. *et al.* (2013) Paclitaxel resistance and multicellular spheroid formation are induced by kallikrein-related peptidase 4 in serous ovarian cancer cells in an ascites mimicking microenvironment. *PLoS ONE*, 8, e57056.

42. Aiello, N.M. *et al.* (2018) EMT subtype influences epithelial plasticity and mode of cell migration. *Dev. Cell*, 45, 681.e4–695.e4.

43. Ehnert, S. *et al.* (2012) Transforming growth factor β1 inhibits bone morphogenic protein (BMP)-2 and BMP-7 signaling via upregulation of Ski-related novel protein N (SnoN): possible mechanism for the failure of BMP therapy? *BMC Med.*, 10, 101.

44. Zeisberg, M. *et al.* (2003) BMP-7 counteracts TGF-beta1-induced epithelial-to-mesenchymal transition and reverses chronic renal injury. *Nat. Med.*, 9, 964–968.

45. Ng, A. *et al.* (2015) Ovary and fimbrial stem cells: biology, niche and cancer origins. *Nat. Rev. Mol. Cell Biol.*, 16, 625–638.

46. Kohan-Ivani, K. *et al.* (2016) Role of dihydrotestosterone (DHT) on TGF-β1 signaling pathway in epithelial ovarian cancer cells. *J. Cancer Res. Clin. Oncol.*, 142, 47–58.

47. Rafehi, S. *et al.* (2016) TGFβ signaling regulates epithelial-mesenchymal plasticity in ovarian cancer ascites-derived spheroids. *Endocr. Relat. Cancer*, 23, 147–159.

48. Sunde, J.S. *et al.* (2006) Expression profiling identifies altered expression of genes that contribute to the inhibition of transforming growth factor-beta signaling in ovarian cancer. *Cancer Res.*, 66, 8404–8412.

49. Cheng, L. *et al.* (2010) Analysis of chemotherapy response programs in ovarian cancers by the next-generation sequencing technologies. *Gynecol. Oncol.*, 117, 159–169.

50. Zhang, S.T. *et al.* (2016) Identification of key genes associated with the effect of estrogen on ovarian cancer using microarray analysis. *Arch. Gynecol. Obstet.*, 293, 421–427.

51. Berry, N.B. *et al.* (2008) Ovarian cancer plasticity and epigenomics in the acquisition of a stem-like phenotype. *J. Ovarian Res.*, 1, 8.

52. Xian, W. *et al.* (2010) The Li-Fraumeni syndrome (LFS): a model for the initiation of p53 signatures in the distal Fallopian tube. *J. Pathol.*, 220, 17–23.

53. Maezawa, Y. *et al.* (2014) Loss of the podocyte-expressed transcription factor Tcf21/Pod1 results in podocyte differentiation defects and FSGS. *J. Am. Soc. Nephrol.*, 25, 2459–2470.

54. Kamble, S. *et al.* (2019) Clinical stratification of high-grade ovarian serous carcinoma using a panel of six biomarkers. *J. Clin. Med.*, 8, 330.